Continuum skin effect in orthotropic elasticity

Aoxi Wang and Chang Qing Chen*
Department of Engineering Mechanics, CNMM and AML, Tsinghua University, Beijing 100084, People's Republic of China

(Received 12 December 2023; revised 18 July 2024; accepted 22 August 2024; published 11 September 2024)

Manifested as the accumulation of bulk eigenstates at open boundaries, non-Hermitian skin effects have been studied extensively in various wave systems with either nonreciprocal couplings or on-site gain/loss effects. Here, by unraveling the space-time duality between the elastostatics of two-dimensional continua and the one-dimensional wave mechanics, we show a non-Hermitian topology inherent in the static deformation response of orthotropic, lossless elastic continua with geometry incompatibility between the fiber alignment and sample construction. The eigenstates of the open boundary system are spatially biased towards the boundary, whose degeneracy and chirality are governed by a spectral winding number unique to continuous systems. The directional accumulation of strain energy within a spatial trajectory excited by a quasistatic load emulates a dynamic skin effect, which can be exploited to program the material deformation response. Our study discloses an underlying non-Hermitian topology in static elastic continua with purely passive modulations, and it sheds light on the exploration of the skin effect in other continuous waveguides.

DOI: 10.1103/PhysRevB.110.104105

I. INTRODUCTION

Spatially periodic structures, either natural crystals with spontaneously ordered atomic arrays or artificial metamaterials with designed microstructures, can be characterized by their band structures and Bloch theorem [1–3]. The lack of periodicity is inevitable for a real material, and it has long been recognized that this boundary effect is negligible for bulk properties such as phonon vibration and charge transport [4–8]. This is also a foundation of the bulk-edge correspondence (BEC) in band topology, which states that the nontrivial bound states of a finite structure can be predicted by the topological invariant defined in the bulk of an infinite system [4,9–12], while the macroscopic bulk states are still extended.

Gain and loss are ubiquitous in nonequilibrium and open dynamic systems, where the time evolution in a short period can be effectively tracked by the non-Hermitian Hamiltonians [13–17]. The invoking of non-Hermiticity brings about intriguing phenomena and at the same time it challenges our understanding of the BEC in the presence of the non-Hermitian skin effect (NHSE), where all bulk eigenmodes for an open boundary condition (OBC) system are localized, and the bulk topological invariant fails to predict the in-gap edge modes [18–25]. In non-Hermitian quantum mechanics, the NHSE is incorporated via an imaginary gauge field [26,27]. On this basis, the skin effect has been observed in other continuous wave systems by synthesizing an effective gauge field, such as optics [28], acoustics [29], and mechanics [30,31], where an active actuation or on-site gain/loss effect is usually employed.

Here, instead of focusing on wave motion, we unveil a non-Hermitian topology inherent in the elastostatics of a fiber-reinforced composite, where the imaginary gauge field is invoked via the geometric mismatch between fiber alignment and sample construction. We show that the directional accumulation of bulk strain energy excited by a quasistatic point load is a static analog of the dynamic skin effect, whereas the boundary localization of bulk states under the semi-infinite boundary condition (SIBC) and the OBC explicitly manifests the skin effect. Our study not only offers an easy-to-implement platform for exploring non-Hermitian physics, as evidenced by the experiments, but it also presents a faithful theory for characterizing localized deformation in anisotropic media.

II. IMAGINARY GAUGE FIELD IN ORTHOTROPIC ELASTICITY

We start with a two-dimensional (2D) homogeneous, orthotropic elastic continuum in the plane-stress state, which can be a single-layered fiber-reinforced composite. The medium extends semi-infinitely in the $x-y$ plane with a boundary at $y = 0$; see Fig. 1. The inclined angle of longitudinal fibers is θ with respect to the horizontal interface. The static bulk mechanical response is governed by the equation of equilibrium $\nabla \cdot \sigma = 0$ with $\boldsymbol{\sigma}$ the Cauchy stress tensor (the body force is neglected). In Voigt notation, the constitutive equation of an orthotropic elasticity is given by

$$\begin{Bmatrix} \sigma_1 \\ \sigma_2 \\ \tau_{12} \end{Bmatrix} = \begin{bmatrix} C_{11} & C_{12} & 0 \\ C_{12} & C_{22} & 0 \\ 0 & 0 & C_{66} \end{bmatrix} \begin{Bmatrix} \varepsilon_1 \\ \varepsilon_2 \\ 2\varepsilon_{12} \end{Bmatrix}, \tag{1}$$

where σ_i and ε_i $(i = 1, 2)$ are the normal stress and strain, τ_{12} and ε_{12} are the shear stress and strain, and C_{ij} is the stiffness coefficients. Note that Eq. (1) is projected on the principal basis along the orthogonal fibers ($x_1 - x_2$ in Fig. 1). The infinitesimal strain tensor is $\varepsilon = \frac{(\nabla u + u\nabla)}{2}$, where $\boldsymbol{u}$ is the

*Contact author: chencq@tsinghua.edu.cn

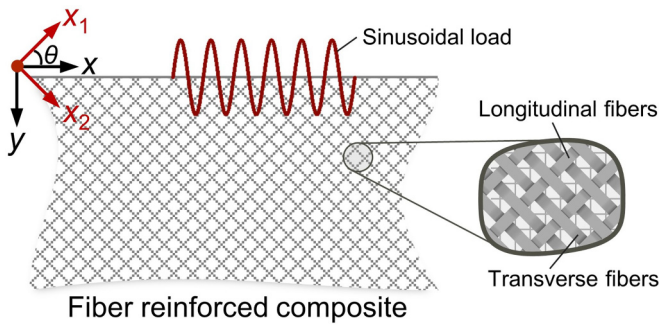

FIG. 1. Schematic of a single-layered fiber-reinforced composite, where the inset shows an enlarged view of the fiber arrangement.

planar displacement field. Combining it with the equilibrium equation and Eq. (1), we obtain the following canonical form resembling Lame's equation for isotropic elasticity [32]:

$$\begin{cases} C_{11}\frac{\partial^2 u_1}{\partial x_1^2} + (C_{12}+C_{66})\frac{\partial^2 u_2}{\partial x_1 \partial x_2} + C_{66}\frac{\partial^2 u_1}{\partial x_2^2} = 0, \\ C_{66}\frac{\partial^2 u_2}{\partial x_1^2} + (C_{12}+C_{66})\frac{\partial^2 u_1}{\partial x_1 \partial x_2} + C_{22}\frac{\partial^2 u_2}{\partial x_2^2} = 0. \end{cases} \tag{2}$$

Suppose the applied displacement load at $y = 0$ has a sinusoidal form and, according to Saint-Venant's principle, it decays exponentially away from the boundary [32], giving rise to the bulk displacement field in the static Rayleigh (SR) form [9,32,33], i.e., $u_y(x, y) = e^{iqx}e^{-\eta y}$ and $u_x(x, y) = cu_y(x, y)$. Here, q is the spatial wave number, η is the decay factor, and c is the polarization. We set $\theta = \pi/4$ in the main text, while leaving the analysis about arbitrary fiber alignment in Ref. [34]. Applying the coordinate transform, we have $u_1 = \xi u_2 = (c-1)/(c+1)u_2$. Then, by combining the two formulas in Eq. (2) and transforming the spatial differential to the natural basis, the following equation can be obtained [34]:

$$\begin{aligned} &\left(C_{11}\xi^2 - C_{66} + C_{66}\xi^2 - C_{22}\right)\left(\frac{\partial^2 u_y}{\partial x^2} + \frac{\partial^2 u_y}{\partial y^2}\right) \\ &+ 2\left(C_{66}\xi^2 - C_{22} - C_{11}\xi^2 + C_{66}\right)\frac{\partial^2 u_y}{\partial x \partial y} = 0. \end{aligned} \tag{3}$$

Under an imaginary gauge transform [19,26], $y = it$, Eq. (3) can be formulated in the form of a wave equation, $i\partial_t u_y = -(\partial_x - b\eta/2a)^2 u_y/\eta + b^2\eta u_y/4a^2$, where a and b are coefficients of C_{ij} [34]. This equation resembles the Schrödinger equation of a 1D spinless particle, i.e., $i\partial_t\psi = -(\partial_x - \beta)^2\psi + V(x)\psi$, where ψ is the wave function, $V(x)$ is the scalar field, and $i\beta$ ($\beta \in \mathbb{R}$) is the imaginary gauge field. This correspondence underlies the duality between the space y in 2D orthotropic elasticity and the time t in 1D nonreciprocal wave systems, and it plays an essential role in the continuum skin effect in fiber-reinforced composites. Furthermore, the involvement of an effective gauge field (i.e., $ib\eta/2a$) relies on the geometrical incompatibility ($\theta \neq 0$ or $\pi/2$), the asymmetric fiber arrangement ($C_{11} \neq C_{22}$), as well as the decaying nature of the SR mode [$\mathrm{Re}(\eta) \neq 0$], which is purely passive.

Applying the SR solution to Eq. (2) decouples ξ and η, yielding the following characteristic equation [34]:

$$\begin{aligned} &[C_{11}(\eta + iq)^2 + C_{66}(\eta - iq)^2][C_{66}(\eta + iq)^2 + C_{22}(\eta - iq)^2] \\ &= (\eta^2 + q^2)^2(C_{12} + C_{66})^2. \end{aligned} \tag{4}$$

Assuming $\eta = \gamma q$ and inserting it into Eq. (4), we obtain a quartic equation about γ. Half of the four bands with $\mathrm{Re}(\eta) > 0$ [$\mathrm{Re}(\eta) < 0$] are decaying (amplifying) modes with the external load applied on the top (bottom) boundary. We focus on the decaying modes in the following.

III. DYNAMIC SKIN EFFECT

It is known that in 1D nonreciprocal wave systems, an inputted wave signal is unidirectionally amplified due to the dynamic skin effect [22,30,35]. Based on the space-time duality, the "wave packet" in our static system is a clustered displacement field incident at the top boundary (serving as the initial state) and evolving along the y axis. Analogous to its dynamic counterpart, the static wave packet behaves as a quasiparticle with a peak location $x_p(y)$ in real space x and a center wave number in reciprocal space q, and it can be excited by a quasistatic point load exerted on the boundary [36]. The difference is that a dynamic wave packet carries the vibration energy in the $1 \oplus 1$D space-time, while a static wave packet localizes the strain energy in 2D spaces. Furthermore, the x-directional skewing rate of the static wave packet during its y-directional state evolution is quantified by the group velocity given by $v_g = \Delta x_p/\Delta y = d\mathrm{Im}(\eta)/dq$, where the gradient of the imaginary decay spectrum is attributed to the imaginary gauge transform.

In continuum elasticity, the stiffness matrix in Eq. (1) must be positive-(semi)definite to avoid a negative strain energy, giving rise to $C_{11}C_{22} \geqslant C_{12}^2$. Since the anomalous material properties depend on the mechanical strength of woven fibers, C_{11} and C_{22}, we set $C_{12} = C_{66} = 1$ for convenience. When $C_{11} = C_{22} = C > 1$, the system preserves the x-reversal symmetry [34], and according to Eq. (4) we have

$$\eta = \pm\sqrt{\frac{-C^2 + 6C + 3 \pm 4\sqrt{-C^3 + 2C^2 + 3C}}{C^2 + 2C - 3}}q = \pm\gamma_{1,2}q. \tag{5}$$

Moreover, $\gamma_{1,2}$ are real numbers when $C \leqslant 3$, implying a vanishing imaginary decay spectrum as well as a zero group velocity, $v_g = 0$; see Fig. 2(a). Therefore, the incident wave packet is confined in the middle bulk region without a bifurcation, emulating a standing wave [3,37]; see Fig. 2(b). By contrast, $\gamma_{1,2}$ become complex when $C > 3$, yielding a pair of imaginary decay spectra with opposite slopes (i.e., $\pm v_g$); see Fig. 2(c). Consequently, the incident wave packet bifurcates into two branches moving towards the left and right boundaries with an equal rate; see Fig. 2(d). The above two situations serve as static analogs of the 1D reciprocal wave motion, corresponding to a trivial non-Hermitian topology. In the limit of $C \to \infty$, we have $\eta \to \pm iq$ and $v_g(q) \to \pm 1$ from Eq. (4), giving rise to $\Delta x_p = \pm\Delta y$ and a static counterpart of the solitary wave [38,39] [Fig. 2(i)]. In another extreme of $C = 1$, we have two sets of solutions: (i) $\eta = 0$, $q = 0$ with

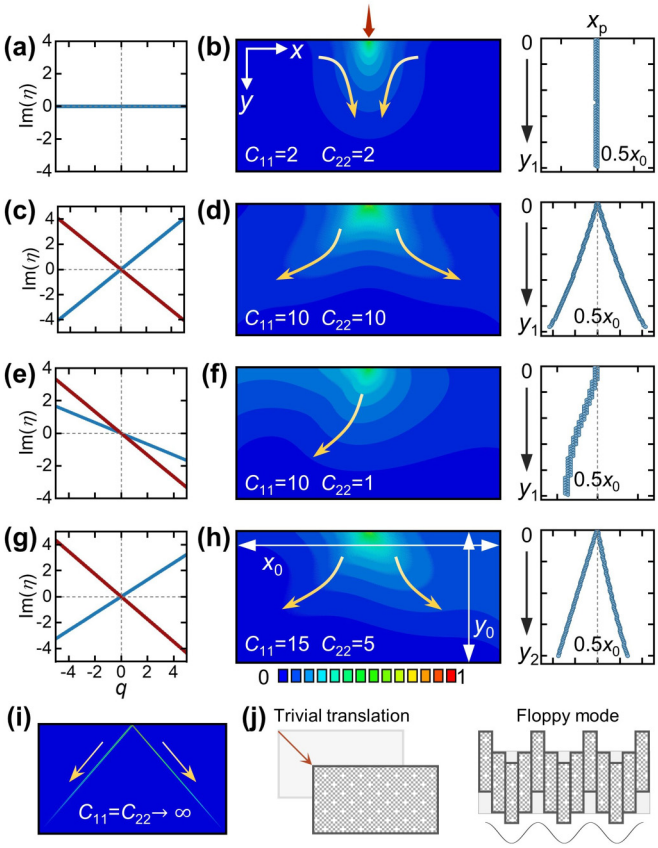

FIG. 2. (a), (c), (e), (g) Imaginary parts of the decay spectrum, which are doubly degenerate. (b), (d), (f), (h) Left panels show the simulated bulk displacement fields under a point load applied at the center of the top boundary (red arrow). Right panels depict the spatial evolution of the wave-packet peaks, $x_p(y)$. (i), (j) Extreme limits for (i) $C \to \infty$ and (j) $C = 1$. Contours in Figs. 2 and 3 denote the displacement magnitude normalized by its corresponding maximum.

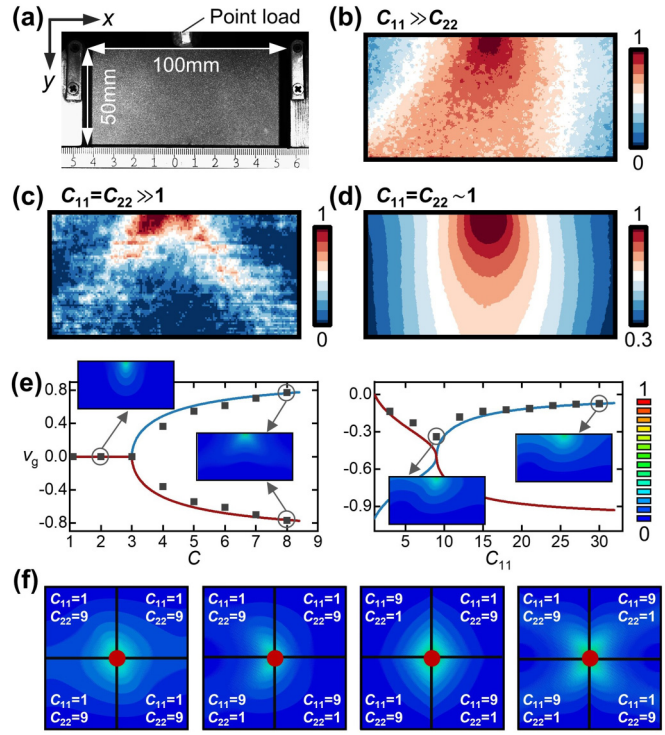

FIG. 3. (a) A typical experimental specimen. (b)–(d) Measured displacement fields of three elastic continua. (e) Simulated group velocities of the symmetric (left panel) and asymmetric (right panel) composites are shown as black squares, with the solid lines denoting the analytical predictions. Insets show the displacement fields with indicated material parameters. (f) Simulated displacement fields in heterostructures composed of four composites, with a point load applied at the junction (red dots). The stiffness coefficients of the constituent parts are labeled in the figure.

arbitrary ξ, and (ii) $\eta = 0, \xi = -1$ (i.e., $u_x = 0$) with arbitrary wave number. The former is the trivial translation, while the latter corresponds to the shear-dominant floppy deformation mode [5]; see Fig. 2(j). For $C_{11} \neq C_{22}$, an either unidirectional or asymmetrically bidirectional transport can be observed, depending on the dispersion of the imaginary decay spectrum, as evident in Figs. 2(e)–2(h). The asymmetric distributions of bulk strain energy excited by a point load are static analogs of the dynamic skin effect, where the incident static wave packet moves towards a biased direction in the physical space x during the evolution along the pseudotime y, and it becomes trivialized when the inclination angle $\theta = 0$ or $\pi/2$, where the effective gauge field vanishes; see Ref. [34].

Experimentally, we have prepared two carbon fiber reinforced epoxy resin composites in a rectangular geometry. One of them is $+45^\circ$ fiber laid (with $C_{11} \gg C_{22}$) while another is $\pm 45^\circ$ fiber laid (with $C_{11} = C_{22} \gg 1$). The material parameters are given in Ref. [34]. A quasistatic point load ($\sim$150 N) towards the $+y$ axis is applied at the middle of the top boundary to excite the static wave packet. The left and right boundaries of the sample are clamped with the bottom boundary fixed; see the photograph in Fig. 3(a). The in-plane displacement fields are measured by the digital-image-correlation method. For the $+45^\circ$ fiber alignment, the measured result reported in Fig. 3(b) implies that the incident wave packet transfers unidirectionally towards the left boundary during spatial evolution, resulting in a deformation concentration at the lower-left corner and mimicking the dynamic skin effect, whereas a bifurcation of the wave-packet trajectory with an almost equal skewing rate towards the left and right boundaries is observed for the $\pm 45^\circ$ fiber alignment, Fig. 3(c), indicating a trivial topology. As a reference, we also prepared an isotropic elastic polymer with the same rectangular geometry, which is topologically equivalent to a symmetric composite with $C_{11} = C_{22} \sim 1$ [34]. The measured displacement field shown in Fig. 3(d) displays a standing-wave characteristic, consistent with Fig. 2(b). The above experiments demonstrate the non-Hermitian topology in orthotropic elasticity, which is easy to implement compared with the wave dynamics [22,30,35,40–42].

The left panel of Fig. 3(e) depicts the C-dependence of the group velocity in symmetric composites, where the transition point $C = 3$ separating the traveling and standing waves is captured. In asymmetric composites with $C_{22} = 1$ and increasing C_{11}, only the upper branch with a small $|v_g|$ is excited, as it attenuates slower compared with another branch and it can be observed in the deep bulk. In this case, a maximum of $|v_g|$ emerges at $C_{11} = 9$; see the right panel of Fig. 3(e). In

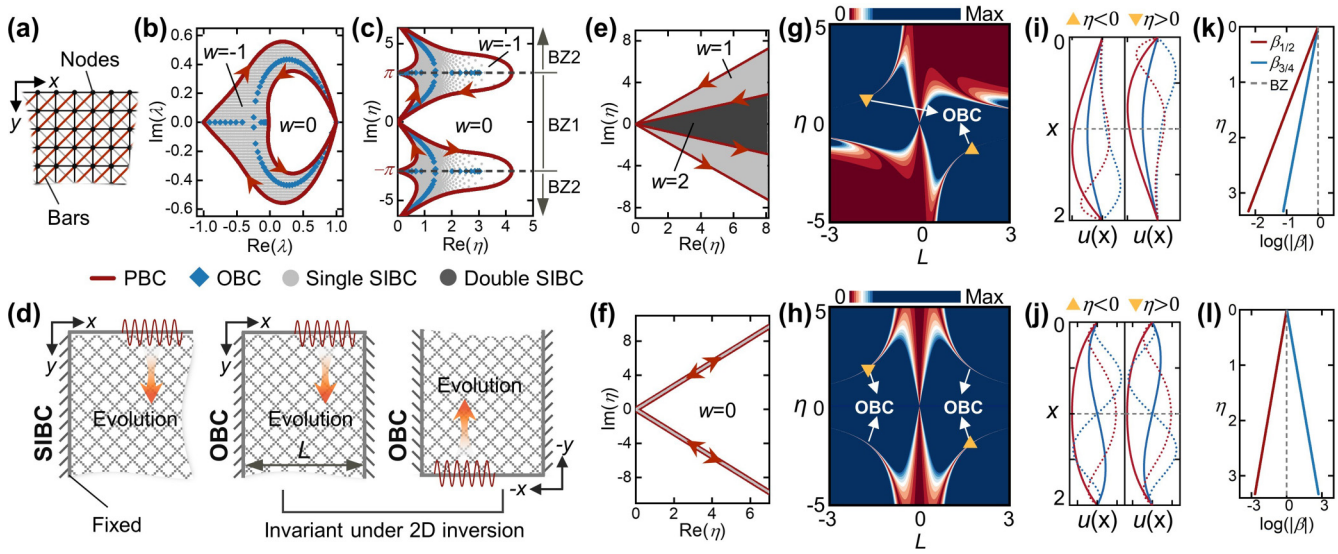

FIG. 4. (a) Lattice discretization of the composite. (b), (c) Corresponding decay spectra of (a) under various boundary conditions, which are projected on the complex (b) λ- and (c) η-planes, respectively. (d) Schematic of a SIBC system and an OBC system. The latter is invariant under the 2D inversion. (e), (f) Decay spectra of orthotropic continua on the η-plane. (g), (h) Contour plots of $|\det J|$ on the η-L plane. (i), (j) Mode profiles of the first-order (solid lines) and third-order (dot lines) OBC eigenstates. (k), (l) Non-Bloch wave numbers of first-order OBC eigenvalues. The parameters are $C_{11} = 10$ and $C_{22} = 1$ for (e), (g), (i), (k), and $C_{11} = C_{22} = 10$ for (f), (h), (j), (l).

addition, the dynamic skin effect in fiber-reinforced composites can be leveraged to pattern the localized deformation modes. Consider a heterostructure composed of four composites with a point load applied at the junction. Figure 3(f) shows the simulated displacement fields for four instances. These deformation modes are ordered, which can be guided to move towards corners (fourth panel) or being trapped by the domain boundaries (third panel), and they are well predicted by the group velocity theory for static wave packets. Additional examples are provided in Ref. [34], where a static analog of the asymmetric negative refraction effect [43] is presented.

IV. POINT-GAP TOPOLOGY

Then, we explicitly solve the spectrum and eigenstates of a continuum with broken translation symmetry along the physical space x. To gain more insight, we first discretize the continuum as a tight-binding model, and we use the Hamiltonian matrix to solve the eigenproblem. An equal-step discretization of Fig. 1 along the x and y axes yields a lattice system, where nodes are arranged in a square array and they are connected by the linking bars; see Fig. 4(a). Here, the horizontal and vertical bars serve as the continuous matrix of the composite, while the diagonal bars are, respectively, the longitudinal and transverse fibers. Furthermore, Eq. (3) corresponds exactly to the nodal equilibrium equation of a lattice in the long-wavelength limit [44]. Applying the SR solution to the lattice equilibrium equation yields a pair of decay spectra, as projected on the complex λ- and η-planes shown in Figs. 4(b) and 4(c), where $\lambda = e^{-\eta}$. Under the x-directional periodic boundary condition (PBC), the bands form closed loops on the complex λ-plane as the wave number traverses the first Brillouin zone (BZ1). For any reference point inside the loop, a point gap [19,20,45] can be well defined, which is labeled by a spectral winding number [20], w; see Fig. 4(b). Conversely, the spectral topology is less visible on the η-plane, as the bands form open arcs rather than closed loops. Nevertheless, because $\mathrm{Im}(\eta) = -\arg(\lambda)$ has a periodicity of 2π, the bands vary periodically along the imaginary axis when the wave number encircles the extended BZ, while eventually converging at $\mathrm{Im}(\eta) = \pm\infty$ when $q = \pm\infty$. On this basis, the point gaps on the complex η-plane are populated within the right area surrounded by the PBC band, and the corresponding winding number depends on the spatial orientation of the adjacent band as the wave number varies from $-\infty$ to ∞ [34], as marked by the red arrows in Fig. 4(c). According to the BEC, any point gap with a nonzero winding number dictates a localized edge state under the SIBC [19]. This is confirmed by the numerically calculated SIBC spectrum, which lies within the nontrivial spectral region with $w = -1$. The OBC spectrum, as derived from a diagonalization of the effective Hamiltonian matrix [34], is also confined in the nontrivial region, and the associated eigenstates are squeezed towards the boundary due to the skin effect.

Under the SIBC, the orthotropic continuum has a truncated boundary at $x = 0$; see Fig. 4(d). Because of the broken x-translational symmetry, the general displacement solution should be taken as a superposition of the four eigenmodes $(q_j(\eta), \xi_j(\eta))$ extracted from Eqs. (3) and (4) for a prescribed η, given by

$$u_y(x,y) = e^{-\eta y}\sum_{j=1}^{4} b_j \beta_j^x,\ u_x(x,y) = e^{-\eta y}\sum_{j=1}^{4} b_j c(\xi_j)\beta_j^x, \quad (6)$$

where $\beta_j = e^{iq_j}$ is the complex wave number with a weight b_j. The fulfillment of the Dirichlet boundary condition [i.e., $u_{x/y}(0,y) = 0$] and the mechanical stability [i.e., $\lim_{x\to\infty} u_{x/y}(x,y) < \infty$] imposes additional constraints on the admissible wave numbers and the concomitant SIBC

spectrum and eigenstates; see the derivations in Ref. [34]. The gray/black dots in Figs. 4(e) and 4(f) mark the singly/doubly degenerate SIBC edge states. For $C_{11} \neq C_{22}$, a remarkable feature of the continuous spectrum is the selective zone-coverage [Fig. 4(e)]. For example, the doubly degenerate SIBC eigenvalues are constrained within the locus embraced by both bands, while the nondegenerate SIBC eigenvalues are populated within the inner region of the two bands. The corresponding SIBC eigenstates are localized at the left boundary. As a natural extension from the lattice system, the right side of each PBC band (red solid lines) on the complex η-plane defines a set of point gaps, whose winding number is governed by the spatial orientation of the left adjacent band when q increases, as marked by the red arrows in Fig. 4(e). Therefore, for point gaps embraced by both bands with the same orientation, the winding number is $w = 1 + 1 = 2$, while for those embraced by only the outer band, the winding number is $w = 1$. In comparison, the two PBC bands are degenerate with opposite orientations when $C_{11} = C_{22}$, giving rise to a countervailing winding number $w = 1-1 = 0$, Fig. 4(f). In this case, the SIBC spectrum overlaps with the PBC bands, and the corresponding eigenstates are extended [34], corroborating its trivial point-gap topology.

Under the OBC, both left ($x = 0$) and right ($x = L$) boundaries of the composite are truncated and fixed [Fig. 4(d)]. Plugging Eq. (6) into the Dirichlet boundary conditions yields four linear equations about b_j, i.e., $\boldsymbol{Jb} = \mathbf{0}$, where $\boldsymbol{b} = (b_1, b_2, b_3, b_4)^T$ and $\mathbf{0}$ is the null vector [34]. The coefficient matrix J is a function of η and L and its determinant should vanish to get a nontrivial solution, i.e., $\det J(\eta, L) = 0$. Hence, for any given system size L, the whole set of OBC eigenvalues η_0 and the associated eigenstates $\boldsymbol{b}_0$ can be resolved by scanning η on the complex plane.

We first investigate the lowest-order OBC solution with a real η_0. Figures 4(g) and 4(h) depict the contour plots of $|\det J|$ on the η-L plane, where the dark red lines mark the OBC spectra respecting $\det J = 0$. The profiles of the lowest-order OBC eigenstates are shown in Figs. 4(i) and 4(j) as the red/blue solid lines for u_y/u_x (with $L = 2$). For $C_{11} \neq C_{22}$, the eigenstate is squeezed towards the left (right) boundary when it evolves along the y ($-y$) axis with $\eta > 0$ ($\eta < 0$), Fig. 4(i), signifying the reciprocal skin effect [19,46] protected by the inherent inversion symmetry of the composite [Fig. 4(d)]. By contrast, the eigenstates are extended with a symmetric spatial configuration when $C_{11} = C_{22}$, Fig. 4(j), compliant with its trivial non-Hermitian topology. In addition to real OBC eigenvalues, there are infinite (yet countable) higher-order modes with complex decay factors and shorter wavelengths for a given size L. All these eigenmodes are localized (extended) when $C_{11} \neq C_{22}$ ($C_{11} = C_{22}$), as exemplified by the dotted lines in Figs. 4(i) and 4(j) for third-order modes. Moreover, the four non-Bloch wave numbers β_j as the constitutions of OBC eigenstates can be extracted to form a generalized Brillouin zone (GBZ) [18,21,47]. In particular, all four β_j have moduli less than 1 when $C_{11} \neq C_{22}$ [Fig. 4(k)], thereby the eigenstates are localized at the left boundary, whereas the wave numbers emerge in reciprocal pairs ($|\beta_{1/2}| = |\beta_{3/4}|^{-1}$) when $C_{11} = C_{22}$ [Fig. 4(l)], for which the eigenstates are delocalized. As is evident, the redefined point-gap and spectral winding number, in terms of the band orientation, restore the BEC in orthotropic continua under both SIBC and OBC. These definitions have been validated in quantum mechanics [27] and acoustics [29] for nonreciprocal wave motions, and they are extended to static continua.

V. CONCLUSION

In summary, we have unveiled the space-time duality between a Cauchy elastostatic continuum with an orthotropic constitutive law and the nonreciprocal wave motion in a lower-dimensional quantum system. On this basis, an effective imaginary gauge field is invoked in fiber-reinforced composites with a geometrical mismatch between the fiber alignment and sample construction, resulting in the emergence of the skin effect. We have demonstrated that the skin effect is explicitly manifested in the selective zone coverage of the SIBC spectrum and the boundary localization of OBC eigenstates, while the asymmetric localization of bulk strain energy under a quasistatic point load signifies a dynamic skin effect. This study advances the exploration of non-Hermitian topology in continuous systems, benefiting from the passive, static characteristic of our systems and the well-established manufacturing technology of engineering composites. Extending this study to 3D laminated plates may allow the chirality of skin modes to be tuned based on different layers.

ACKNOWLEDGMENT

We thank Laibin Zhang and Guowen Wang for help in experiments. This work is supported by the National Natural Science Foundation of China (No. 12132007 and No. 11921002).

[1] A. H. Castro Neto, F. Guinea, N. M. R. Peres, K. S. Novoselov, and A. K. Geim, The electronic properties of graphene, Rev. Mod. Phys. **81**, 109 (2009).

[2] F. D. M. Haldane and S. Raghu, Possible realization of directional optical waveguides in photonic crystals with broken time-reversal symmetry, Phys. Rev. Lett. **100**, 013904 (2008).

[3] M. I. Hussein, M. J. Leamy, and M. Ruzzene, Dynamics of phononic materials and structures: Historical origins, recent progress, and future outlook, Appl. Mech. Rev. **66**, 040802 (2014).

[4] M. Z. Hasan and C. L. Kane, Colloquium: Topological insulators, Rev. Mod. Phys. **82**, 3045 (2010).

[5] C. L. Kane and T. C. Lubensky, Topological boundary modes in isostatic lattices, Nat. Phys. **10**, 39 (2014).

[6] C. L. Kane and E. J. Mele, Z_2 Topological order and the quantum spin Hall effect, Phys. Rev. Lett. **95**, 146802 (2005).

[7] F. Guinea, M. I. Katsnelson, and A. K. Geim, Energy gaps and a zero-field quantum Hall effect in graphene by strain engineering, Nat. Phys. **6**, 30 (2010).

[8] N. Okuma and M. Sato, Non-Hermitian skin effects in Hermitian correlated or disordered systems: Quantities sensitive or insensitive to boundary effects and pseudo-quantum-number, Phys. Rev. Lett. **126**, 176601 (2021).
[9] A. Wang, Y. Zhou, and C. Q. Chen, Topological mechanics beyond wave dynamics, J. Mech. Phys. Solids **173**, 105197 (2023).
[10] Y. Zhou, Y. Zhang, and C. Q. Chen, Amplitude-dependent boundary modes in topological mechanical lattices, J. Mech. Phys. Solids **153**, 104482 (2021).
[11] P. Wang, L. Lu, and K. Bertoldi, Topological phononic crystals with one-way elastic edge waves, Phys. Rev. Lett. **115**, 104302 (2015).
[12] M. Xiao, G. Ma, Z. Yang, P. Sheng, Z. Q. Zhang, and C. T. Chan, Geometric phase and band inversion in periodic acoustic systems, Nat. Phys. **11**, 240 (2015).
[13] R. El-Ganainy, K. G. Makris, M. Khajavikhan, Z. H. Musslimani, S. Rotter, and D. N. Christodoulides, Non-Hermitian physics and PT symmetry, Nat. Phys. **14**, 11 (2018).
[14] Y. Ashida, Z. Gong, and M. Ueda, Non-Hermitian physics, Adv. Phys. **69**, 249 (2020).
[15] E. J. Bergholtz and J. C. Budich, Exceptional topology of non-Hermitian systems, Rev. Mod. Phys. **93**, 015005 (2021).
[16] S. Weimann, M. Kremer, Y. Plotnik, Y. Lumer, S. Nolte, K. G. Makris, M. Segev, M. C. Rechtsman, and A. Szameit, Topologically protected bound states in photonic parity–time-symmetric crystals, Nat. Mater. **16**, 433 (2017).
[17] F. Song, S. Yao, and Z. Wang, Non-Hermitian skin effect and chiral damping in open quantum systems, Phys. Rev. Lett. **123**, 170401 (2019).
[18] S. Yao and Z. Wang, Edge states and topological invariants of non-Hermitian systems, Phys. Rev. Lett. **121**, 086803 (2018).
[19] N. Okuma, K. Kawabata, K. Shiozaki, and M. Sato, Topological origin of non-Hermitian skin effects, Phys. Rev. Lett. **124**, 086801 (2020).
[20] Z. Gong, Y. Ashida, K. Kawabata, K. Takasan, S. Higashikawa, and M. Ueda, Topological phases of non-Hermitian systems, Phys. Rev. X **8**, 031079 (2018).
[21] K. Yokomizo and S. Murakami, Non-bloch band theory of non-Hermitian systems, Phys. Rev. Lett. **123**, 066404 (2019).
[22] Q. Liang, D. Xie, Z. Dong, H. Li, H. Li, B. Gadway, W. Yi, and B. Yan, Dynamic signatures of non-Hermitian skin effect and topology in ultracold atoms, Phys. Rev. Lett. **129**, 070401 (2022).
[23] V. M. Martinez Alvarez, J. E. Barrios Vargas, and L. E. F. Foa Torres, Non-Hermitian robust edge states in one dimension: Anomalous localization and eigenspace condensation at exceptional points, Phys. Rev. B **97**, 121401(R) (2018).
[24] T. E. Lee, Anomalous edge state in a non-Hermitian lattice, Phys. Rev. Lett. **116**, 133903 (2016).
[25] C. H. Lee and R. Thomale, Anatomy of skin modes and topology in non-Hermitian systems, Phys. Rev. B **99**, 201103(R) (2019).
[26] N. Hatano and D. R. Nelson, Localization transitions in non-Hermitian quantum mechanics, Phys. Rev. Lett. **77**, 570 (1996).
[27] S. Longhi, Non-Hermitian skin effect beyond the tight-binding models, Phys. Rev. B **104**, 125109 (2021).
[28] K. Yokomizo, T. Yoda, and S. Murakami, Non-Hermitian waves in a continuous periodic model and application to photonic crystals, Phys. Rev. Res. **4**, 023089 (2022).
[29] W. Cheng and G. Hu, Acoustic skin effect with non-reciprocal willis materials, Appl. Phys. Lett. **121**, 041701 (2022).
[30] Y. Chen, X. Li, C. Scheibner, V. Vitelli, and G. Huang, Realization of active metamaterials with odd micropolar elasticity, Nat. Commun. **12**, 5935 (2021).
[31] C. Scheibner, A. Souslov, D. Banerjee, P. Surówka, W. T. M. Irvine, and V. Vitelli, Odd elasticity, Nat. Phys. **16**, 475 (2020).
[32] E. G. Karpov, Structural metamaterials with Saint-Venant edge effect reversal, Acta Mater. **123**, 245 (2017).
[33] A. Wang, Z. Meng, and C. Q. Chen, Non-Hermitian topology in static mechanical metamaterials, Sci. Adv. **9**, eadf7299 (2023).
[34] See Supplemental Material at http://link.aps.org/supplemental/10.1103/PhysRevB.110.104105 for additional details.
[35] M. Brandenbourger, X. Locsin, E. Lerner, and C. Coulais, Non-reciprocal robotic metamaterials, Nat. Commun. **10**, 4608 (2019).
[36] E. G. Karpov, L. A. Danso, and J. T. Klein, Anomalous strain energy transformation pathways in mechanical metamaterials, Proc. R. Soc. Math. Phys. Eng. Sci. **475**, 20190041 (2019).
[37] S. Weidemann, M. Kremer, T. Helbig, T. Hofmann, A. Stegmaier, M. Greiter, R. Thomale, and A. Szameit, Topological funneling of light, Science **368**, 311 (2020).
[38] H. Xiu, I. Frankel, H. Liu, K. Qian, S. Sarkar, B. MacNider, Z. Chen, N. Boechler, and X. Mao, Synthetically non-Hermitian nonlinear wave-like behavior in a topological mechanical metamaterial, Proc. Natl. Acad. Sci. USA **120**, e2217928120 (2023).
[39] Y. Zhang, B. Li, Q. S. Zheng, G. M. Genin, and C. Q. Chen, Programmable and robust static topological solitons in mechanical metamaterials, Nat. Commun. **10**, 5605 (2019).
[40] L. Zhang *et al.*, Acoustic non-Hermitian skin effect from twisted winding topology, Nat. Commun. **12**, 6297 (2021).
[41] T. Helbig, T. Hofmann, S. Imhof, M. Abdelghany, T. Kiessling, L. W. Molenkamp, C. H. Lee, A. Szameit, M. Greiter, and R. Thomale, Generalized bulk–boundary correspondence in non-Hermitian topolectrical circuits, Nat. Phys. **16**, 747 (2020).
[42] A. Ghatak, M. Brandenbourger, J. van Wezel, and C. Coulais, Observation of non-Hermitian topology and its bulk–edge correspondence in an active mechanical metamaterial, Proc. Natl. Acad. Sci. USA **117**, 29561 (2020).
[43] S. Zanotto, G. Biasiol, P. V. Santos, and A. Pitanti, Metamaterial-enabled asymmetric negative refraction of GHz mechanical waves, Nat. Commun. **13**, 5939 (2022).
[44] A. Wang and C. Q. Chen, Stress guides in generic static mechanical metamaterials, Natl. Sci. Rev. nwae110 (2024).
[45] K. Kawabata, K. Shiozaki, M. Ueda, and M. Sato, Symmetry and topology in non-Hermitian physics, Phys. Rev. X **9**, 041015 (2019).
[46] T. Hofmann *et al.*, Reciprocal skin effect and its realization in a topolectrical circuit, Phys. Rev. Res. **2**, 023265 (2020).
[47] K. Zhang, Z. Yang, and C. Fang, Correspondence between winding numbers and skin modes in non-Hermitian systems, Phys. Rev. Lett. **125**, 126402 (2020).